



# CFD ANALYSIS OF THE ZIMMERMAN'S V173 STOL AIRCRAFT

Luca Piancastelli<sup>1</sup>, Alfredo Gatti<sup>2</sup>, Leonardo Frizziero<sup>1</sup>, Lena Ragazzi<sup>1</sup> and e Marco Cremonini<sup>3</sup>

<sup>1</sup>Alma Mater Studiorum University of Bologna, Department of Industrial Engineering, Viale Risorgimento, Bologna, Italy

<sup>2</sup>Alenia Aermacchi, A Finmeccanica Company, Piazza Monte Grappa, Rome, Italy

<sup>3</sup>Nuovamacut TeamSystem Group, Via E. Majorana, Reggio Emilia, Italy

E-Mail: [leonardo.frizziero@unibo.it](mailto:leonardo.frizziero@unibo.it)

## ABSTRACT

The present work had as its main aim to carry out a study of the high lift of an unconventional aircraft of the '40s, the Vought V-173 Flying Pancake. To obtain this result the Authors used the Computational Fluid Dynamics (CFD) software SolidWorks Flow Simulation. In particular, the  $C_L$ - $\alpha$  and  $C_D$ - $\alpha$  curves have been interpolated from the points obtained from the simulations for different configurations of the V173 aircraft CAD model. In a first phase the aerodynamics of the aircraft was evaluated 'clean' without the presence of the propellers was analysed. In a second phase, the influence of the two large propellers was taken into account. The effect of the propeller was clearly shown especially at high AOA. These results were obtained from the direct comparison of the Lift-AOA and Drag-AOA curves for the unpowered and the powered condition. The CFD results confirmed the impression of high controllability of the powered aircraft up to AOA of 50°. This behavior with the extremely smooth stall gave the impression of an aircraft impossible to stall or to spin.

**Keywords:** CFD, CAD, STOL, V173, flying pancake.

## INTRODUCTION

Charles H. Zimmerman worked on his "Flying Pancake" design from 1933 to 1937. At that time he was a researcher at the National Advisory Committee for Aeronautics (NACA) at Langley Field. He was granted patent #2, 108, 093 on February 14, 1938. The future "Flying Pancake" was to be the optimum configuration for high-speed aircrafts. The design promised high speed with low take-off speed. One of the benefits of Zimmerman's design was that the entire aircraft generated lift. A streamline, flat-body flying-wing enclosed the load and the power plants with other accessories. Hence, its cross section is bi-elliptical rather than round, efficiently to provide lift at high speeds. This double elliptical cross-sectional shape provided also an effective dihedral angle on the lower surface. The fore-and-aft contour secured a smooth, substantially undisturbed flow of air over the aerial vehicle. Drag optimization required that the pilot and passengers occupy a prone position in the depth of the body in smaller machines. It was understood that the enclosure for the pilot and payload may be suitably faired into the adjacent part of the surface of the craft. According to Zimmerman, this position is by far the most comfortable in case of airsickness. The location of the propellers at the wing tips increased the aerodynamic efficiency above that of other aircraft of the same span loading. The rotation of the tip-wing propellers is arranged in such directions that most of the energy, which would otherwise be lost in twist of the slipstream, is returned to the machine in the form of diminished induced drag. Hence, the wing-tip propellers are installed in such a way that their rotation meet on the upward turn. In this way, the energy normally wasted in the twist of the slipstream is partially recovered. In fact, the propellers wake counteracts the formation of wing-tip

vortices and reduces the very considerable induced drag due to such vortices. These positions and directions of rotation of the propellers result in an increase of the effective wingspan. Other modern aerial vehicles, for example by the V22 Osprey, retrieve this feature. Two interconnected engines were used to make single engine flight possible. The propellers were of the controllable-pitch type so that they could have a low pitch when taking off and a higher pitch for high speed, horizontal flight. Torque and gyroscopic couples are neutralized. The slipstream velocity of the propeller is designed to be always in the range of 26 to 45 mps, so that the control surfaces will be very effective even in low-speed flight. The relatively high wing loading improves the handling of the vehicle at low speed, when changes in wind direction will produce much less violent changes in attitude or velocity of the craft. Zimmerman joined United's Chance Vought Aircraft Division in 1937 as project engineer. The Navy initiated development of the Flying Flapjack with award of contract to Vought-Sikorsky for design of the VS-173, based upon the research of Zimmerman, on 27 February 1940. Wind tunnel tests on full scale models being done in 1940-41. On 23 November 1942 Chance Vought test pilot, Boone T. Guyton, took the V-173 "Flying Flapjack" research aircraft into the air. The V-173, flown many times, was capable of very short take-offs and landings. Among the few incidents in these testing phases remembers the crash landing of the pilot Charles Lindbergh that overturned when the aircraft was at very low speed. The 16.5-foot-diameter wooden propellers were so large that the aircraft rested at a 22-degree-upward angle, forcing the pilot to look through the windows at his feet when taking off or landing. The flying pancake behaved more or less like a V-22 Osprey with its large propellers spinning at relatively high velocities as well, which wind up with very large



gyroscopic forces. Even the propeller blades were articulated similarly to the movements of the rotors on a helicopter. The control system of the V173 consisted of a pair of conventional vertical stabilizers on the symmetrical air foil. Between the stabilizers, two stability flaps were installed. Pitch and roll were achieved with a pair of ailerons-combination ailerons and elevators located on the edges of the wing like body. It is documented that Zimmerman's STOL (Short Take off Landing) design could achieve a zero-roll take-off with a 25-knot headwind. Tested for a total of 131 hours, this full-scale prototype substantially confirmed Zimmermann's theoretical work. The aircraft was so underpowered that the engines could barely keep the craft in the air and the stick forces were extremely heavy due to the lack of hydraulic servos. The overall handling and performance were sluggish. However, the take-off-landing run was only 15 m. The final working version was completed in 1947. The XF5U-1 was very similar to the V-173 but of metal/metalite construction. The metalite was a sandwich structure with a very thin core of balsa wood bonded between two skins of very strong aluminium. Two 1,600HP Pratt and Whitney R-2000-7 engines were buried in the "wing" on either side of the cockpit, cooled by air inlets on the leading-edge and driving two large four-bladed propellers with articulated blades like those of a helicopter, through a complicated transmission system. The control surfaces consisted of twin fins and rudders and between them were sited wide flaps; all moving horizontal tail planes and elevators were sited outboard of the vertical tail planes. The retractable landing gear was unusually high. It was designed to climb 5,000 feet in 7 minutes. It should achieve a the maximum speed of 460 mph with a stall speed of 20 mph. Projecting even further, two turbo shafts of the time (1949) should provide a maximum speed of 550 mph with near zero stall speed. With the turboprops, the XF5 U-1 would actually hover motionless in the air, hanging under its props like a helicopter. The NACA 0015 flying wing structure was built entirely of fabric-covered-wood to reduce weight and increase the efficiency, even if its manufacturing was challenging and complicated. Starting from the circle, its wing plant can be seen as a sum of two ellipses: (Figure-1).(L. Piancastelli & A. Gatti)

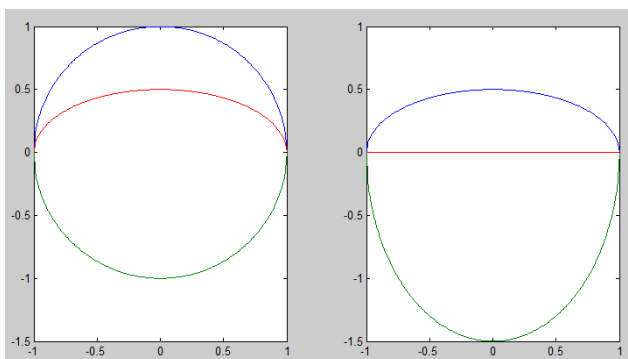


**Figure-1.** V173 bi-elliptical profile from a circle.

### CFD implementation

High quality, complete and accurate CAD 3D models are the starting point for all virtual prototyping and physical simulations. These data form the bulk of the Product Lifecycle Management (PLM) that is widely deployed by many industries. PLM is the tool by which 3D manufactured product data are used and maintained during an entire product's lifecycle and across all its design changes.

The combined use of Computational Fluid Dynamics, (CFD) and FE (Finite Element) in CAD-centred system can significantly accelerate the design process. However, this process may have a drawback of increasing design complexity. This fact unavoidably increases the dependence on external "specialized" development partners for simulation and optimization. The continuous improvement of CAD-embedded FSI (Fluid System Interaction) software packages has progressively reduced the necessity for these external partners. These software packages are designed to keep pace with the unavoidable design development. The geometry changes are followed by engineering simulations, interpretations and optimizations. To make FSI usable for mechanical designers and design engineers from other engineering disciplines, CFD software package have been largely automated to minimize the specialist expertise required to operate traditional CFD software. The capabilities of CAD-embedded CFD to handle fairly complex geometries and also to simulate complex industrial turbulent flows with heat and mass transfer is then extremely important, together with simulation's turbulence capabilities.

Nowadays, even our CAD-embedded Flow Simulation software is a 10 years old mature code with thousand man-years of development effort behind it [1]. It utilizes a modified  $k-\epsilon$  two-equation turbulence model optimized for a wide range of turbulence scenarios. An immersed boundary Cartesian meshing techniques allow for fairly accurate flow field resolution with low cell mesh densities [2] (Figure-2).(L. Frizziero & L. Ragazzi)

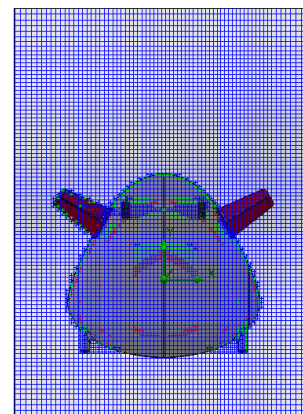


**Figure-2.** CFD Immersed boundary Cartesian mesh [3].

The immersed boundary methods are fairly simple. At first, the pre-processor detects the



computational cells that are cut by the body. The cells are then divided in those that are inside and outside of the body.

The cut cells are separated in two types of cells corresponding to the location of their cell center. The cells that have their geometrical center outside or on the surface of the body are labeled as interface cells. The other cut cells are treated like inside cells.

The flow variable  $\phi$ , which represents a turbulence variable, is set to zero in the inside cells.

At the interface cells, the nearby wall is modeled with an off wall boundary condition which in general consists of a linear interpolation pattern corrected with a (non-linear) correction.

The scalar variable  $\phi$  in the interface cell ( $i,j$ ) is interpolated in two steps, using only the neighboring cells that are further away from the body. Initially, a linear interpolation is carried out along the normal to the wall up to an intermediate location that has the same distance to the wall as the interface cell center ( $i,j$ ) for each neighboring cell. The second interpolation takes on a surface that is parallel to the wall. Here, the inverse-distance weighted method proposed by Franke (1982) [4] that preserve local maxima and produces smooth reconstructions. The interpolation of  $\phi(i,j)$  in the interface cell is:

$$\phi_{(i,j)} = \sum_m \frac{w_m \phi_m}{q} \quad (1)$$

with

$$w_m = \left( \frac{H - h_m}{H \times h_m} \right)^2 \quad (2)$$

and

$$q = \sum_m w_m, m = \{N, S, E, W\} \quad (3)$$

where  $\phi_m$  are the previously interpolated values,  $h_m$  is the distance between the position of  $\phi(i,j)$  and the position of  $\phi_m$  and  $H$  is the maximum of the values of  $h_m$ .

The sum is over the neighboring cells, with  $m$  that identify the cell over (N-Nord), under (S-South) on the left (E-East) and on the right (W-West) of the current cell. The weights  $w_m=0$  for all non-qualifying neighbors. For each interface cell the described linear interpolation results in a set of weights  $\beta_m$  which summarize the effect of each neighbor cells on the interface cell:

$$\phi_{(i,j)} = \beta_W \phi_W + \beta_E \phi_E + \beta_S \phi_S + \beta_N \phi_N \quad (4)$$

By considering only the neighboring cells (W, E, S, N) that have a common face with the interface cell ( $i,j$ ) the linear interpolation (4) can easily be treated in an implicit way. In fact, in the computational CFD RANS (Reynolds Averaged Navier-Stokes) code, a second-order, implicit, cell centered Cartesian mesh is used within a pressure-velocity coupling algorithm with a segregated solution of the field equations [5]. These equations are discretized in three-dimensions with a 7-point pattern. However, in this brief introduction, we will refer for simplicity to the corresponding two-dimensional equations. Therefore, for each cell ( $i,j$ ), the discretized field equation for momentum, turbulent scalar and pressure correction can be written as:

$$a_W^n \phi_W^{n+1} + a_E^n \phi_E^{n+1} + a_S^n \phi_S^{n+1} + a_N^n \phi_N^{n+1} = s_{(i,j)}^n \quad (5)$$

The implicit matrix of the equation (5) can be modified with the weights  $\beta_m$  without introducing new diagonals with non-zero elements. However, the inclusion of geometrical singular points such as corners should be done explicitly. For a non-linear near wall behavior of  $\phi$  an explicit correction  $\Delta\phi_{\text{corr}}$  is added to the right hand side of equation (4). This mesh generator can be used in conjunction with Van Driest's (1956) universal profiles. These profiles can be used to describe two classes of turbulent boundary layers. The thick boundary layer model is used when the fluid mass centers of the near-wall mesh cells are located inside the boundary layer. The thin boundary layer model substitutes the first one when the fluid mass centers of the near-wall mesh cells are located outside the boundary layer. These boundary layer models overcome the problem of a very fine mesh density near the walls in the calculation. The Launder Spalding functions specify the wall boundary conditions for the RANS in an enhanced turbulence  $k-\epsilon$  model. In the other regions of the computational domain the  $k-\epsilon$  with damping model of Lamand Brethorst [6] describes laminar, turbulent, and transitional flows of homogeneous fluids consisting of turbulence energy conservation equations (6) (7).

$$\frac{\partial \rho k}{\partial t} + \frac{\partial \rho k u_i}{\partial x_i} = \frac{\partial}{\partial x} \left( \left( \mu + \frac{\mu}{\sigma_k} \right) \frac{\partial k}{\partial x} + \tau_{ij}^R \frac{\partial u_i}{\partial x_j} - \rho \epsilon + \mu_i P_B \right) \quad (6)$$

$$\frac{\partial \rho \epsilon}{\partial t} + \frac{\partial \rho \epsilon u_i}{\partial x_i} = \frac{\partial}{\partial x} \left( \left( \mu + \frac{\mu}{\sigma_k} \right) \frac{\partial \epsilon}{\partial x} + C_{11} \frac{\epsilon}{k} \left( f_1 \tau_{ij}^R \frac{\partial u_i}{\partial x_j} + \epsilon_1 \mu_i P_B \right) - f_2 C_{12} \frac{\rho \epsilon^2}{k} \right) \quad (7)$$

With

$$\tau_{i,j} = \mu s_{ij}, \tau_{i,j}^R = \mu_i s_{ij} - \frac{2}{3} \rho_k \delta_{ij},$$

$$s_{ij} = \frac{\partial u_i}{\partial x_j} + \frac{\partial u_j}{\partial x_i} - \frac{2}{3} \delta_{ij} \frac{\partial u}{\partial x_k}, P_B = - \frac{g_i}{\sigma_B \rho} \frac{\partial \rho}{\partial x_i}$$



where  $C_{ij}=0.09$ ,  $C_{i1}=1.44$ ,  $C_{i2}=1.92$ ,  $\sigma_k=1$ ,  $\sigma_\epsilon=1.3$ ,  $\sigma_B=0.9$  and  $C_B=1$  or  $C_B=0$  for  $P_B>0$  and  $P_B<0$ .

Lam and Bremhorst's damping function are used in the turbulent viscosity term (8) (9).

$$f_\mu = \left(1 - e^{-0.025R_y}\right)^2 \left(1 + \frac{20.5}{R_t}\right) \quad (8)$$

$$\mu_t = f_\mu \left( \frac{C_\mu \rho k^3}{\epsilon} \right) \quad (9)$$

$y$  is the distance of the point from the wall, and

$$R_y = -\frac{\rho y \sqrt{k}}{\mu}, \quad R_t = -\frac{\rho k^2}{\mu \epsilon}$$

Lam and Bremhorst's damping functions  $f_\mu$ ,  $f_1$ ,  $f_2$  decrease turbulent viscosity and turbulence energy and increase the turbulence dissipation rate. These parameters are controlled by the Reynolds number  $R_y$ .  $R_y$  is calculated on the average velocity of fluctuations and distance from the wall. When  $f_\mu = 1$ ,  $f_1 = 1$ ,  $f_2 = 1$  the approach obtains the original  $k$ - $\epsilon$  model.

A fluid's boundary layer requires a very high density mesh to give accurate results. This approach impairs the computational efficiency of the simulation and usually requires long computer time on extremely performing computing systems. For this reason the computational mesh used in our CFD code is always an immersive boundary non-body-fitted Cartesian mesh. For this purpose the dimensionless distance parameter from the wall parameter  $y^+$  is used (10).

$$y^+ = \frac{y \sqrt{\tau_w k}}{\mu} \quad (10)$$

Therefore, the dimensionless distance from the turbulent equilibrium region's outer boundary up to  $y^+=300$  follows the experimental data presented by Wilcox (1994) [7]. With this approach the CFD explicitly obtains the momentum, heat flux, and turbulent boundary conditions for the RANS. This approach simplifies the mesh and reduces the computational time even in large domains. It is then possible to obtain fairly accurate results with standard desktop computers. (L. Piancastelli et al.)

### CFD simulations on the V173

Many simulations were performed to build the  $CD/CL$ - $\alpha$  (Angle Of Attack) curves. For each simulation the AOA was varied by varying the boundary condition  $v_y$  (horizontal component of air speed) and  $v_z$  (vertical

component of air speed) with constant  $TAS=U=50$  m/s (True Air Speed).

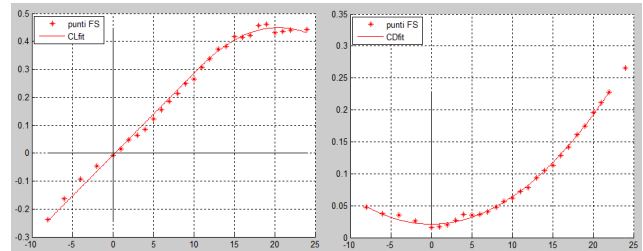


**Figure-3.** V173  $C_L/C_D$ -AOA curves from CFD analysis "Punti FS".

The environmental conditions were set to ISA+0, 1200m s.l. It is then possible to obtain the values of  $CL$  and  $CD$  from equations (11, 12, 13, 14)

$$L = F_z \cos(\alpha) - F_y \sin(\alpha) \quad (11)$$

$$D = F_z \sin(\alpha) + F_y \cos(\alpha) \quad (12)$$

$$C_L = \frac{F_z \cos(\alpha) - F_y \sin(\alpha)}{\frac{1}{2} \rho S U_\infty^2} \quad (13)$$

$$C_D = \frac{F_z \sin(\alpha) + F_y \cos(\alpha)}{\frac{1}{2} \rho S U_\infty^2} \quad (14)$$

The curves  $C_D/C_L$ - $\alpha$  of the V173 without propeller are shown in Figure 3.

The  $C_L$  curve passes through the origin and the stall is close to of  $20^\circ$ , with a maximum value of  $C_L$  between 0.4-0.5.

The  $C_D$  curve is approximately symmetric to the origin.

It was decided to perform the CFD tests the speed of maximum efficiency  $V_{E_{max}}=V_{cruise}$ . This value is lower than the true best efficiency of the V173. This fact is due to the contribution of the propeller wake to drag reduction. The starting data are: the V173 mass  $W = 1020.21$  k, the curves of Figure-3 and the air density at the flight altitude (1200 m,  $\rho = 1.09$  kg/m<sup>3</sup>). The velocity of maximum efficiency  $V_{E_{max}} \approx 50$  m/s can be obtained with equations (15, 16 and 17).

$$\frac{d}{d\alpha} \left( \frac{C_L}{C_D} \right) = \frac{d}{d\alpha} \left( \frac{C_{L0} + \alpha C_{L\alpha}}{\alpha^2 + b\alpha + c} \right) = 0 \quad (15)$$

$$\alpha_{E_{max}} = \frac{-\alpha C_{L0} + \sqrt{a^2 C_{L0}^2 + a c C_{L\alpha}^2 - a b C_{L0} C_{L\alpha}}}{a C_{L\alpha}} = 8.2^\circ \quad (16)$$

$$V_{E_{max}} = \sqrt{\frac{2W}{\rho S C_{L_{E_{max}}}}} = \sqrt{\frac{2W}{\rho S (C_{L0} + \alpha_{E_{max}} C_{L\alpha})}} = 47.5 \frac{m}{s} \quad (17)$$





In absence of the data about the V173 propellers a new design was performed. The known data are summarized in Table-1:

**Table-1.** Propellers data.

Description	Symbol	Value	Unit
Number of propellers	B	2	-
Number of blades	N	3	-
Propeller diameter	D	5	m
Spinner diameter	-	0.324	m
Maximum motor power	Pmax	60	kW

The airfoil chosen for the propellers is the Clark Y. The other problem is to choose the right rotational speed for the propeller. It is known that the max TAS (True Air Speed) is  $V_a=61\text{m/s}$  sea level. At this TAS the engine should run at full power (100% rpm). It has been assumed that a reasonable value for propeller tip speed is  $V_t = 0.91M=309.7\text{m/s}$  ISA+0. The rotational speed of the propeller is then  $n_{\max}\approx 1150\text{ rpm}$  (18) (19).

$$V_t = \sqrt{V_r^2 - V_a^2} = 303.6\text{ m/s} \quad (18)$$

$$n_{\max} = \frac{V_t}{\pi D} 60 = 1159\text{ rpm} \quad (19)$$

It was chosen to design a twisted propeller with the Theodorsen method. The input parameters are summarized in Table-2.

**Table-2.** Input data for propeller design.

Description	Symbol	Value	Unit
Propeller diameter	D	5	m
# of blades	N	3	-
Design velocity aircraft	$V_a$	61	m/s
Design lift coefficient of the airfoil (Clark Y)	$C_{L\text{propdesign}}$	1	-
Rotational speed	nmax	1150	rpm
Power	Pmax	60	kW

The Theodorsen-Crieg methods requires to calculate the advance ratio  $\lambda$  (20) (21), where  $w$  is the rearward displacement velocity of the helical vortex surface. In our case the term  $\bar{w}$  in equation (21) can be neglected.

$$\bar{w} = \frac{w}{V} = 0.05 \quad (20)$$

$$\lambda = \frac{V}{nD} (1 + \bar{w}) \approx \frac{V}{nD} \quad (21)$$

### V173 performance curve at cruise speed (50 m/s)

From the simulations, the  $C_L$ - $\alpha$  curve is almost linear up to  $40^\circ$  (Figure 4). After the AOA of  $40^\circ$ , the curve loses its linearity up to the peak of  $51.4^\circ$ . The loss of lift after this peak is not abrupt, as typical of low aspect ratio wings. This fact explains the feeling of "being impossible to stall".

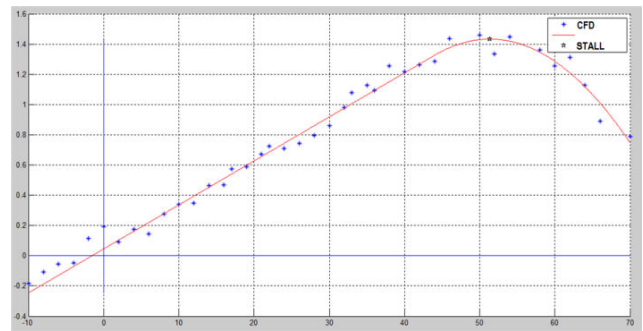


**Figure-4.**  $C_L$ -  $\alpha$  curve is almost linear up to  $40^\circ$ .

The  $C_D$ - $\alpha$  curve is almost parabolic up to  $\alpha = 40^\circ$ . At this point, the stall begins and the curve loses of significance.

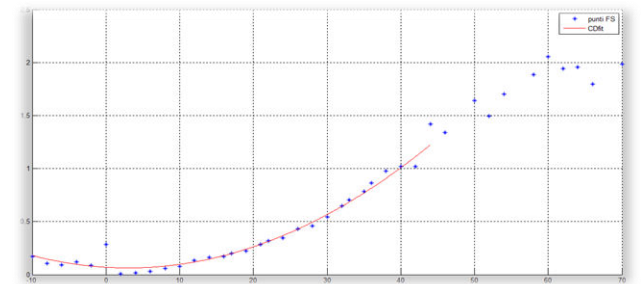


**Figure-5.**  $C_D$ -  $\alpha$  curve is almost parabolic up to  $40^\circ$ .

The curve is in agreement with the fact that the  $C_D$  is parabolic (Figure-5) and symmetric about the y axis for a symmetrical profile as the NACA 0015 (used for the Pancake). The presence of the propellers wake seems to improve the overall performance by improving the effective span length. (L. Piancastelli & M. Cremonini)

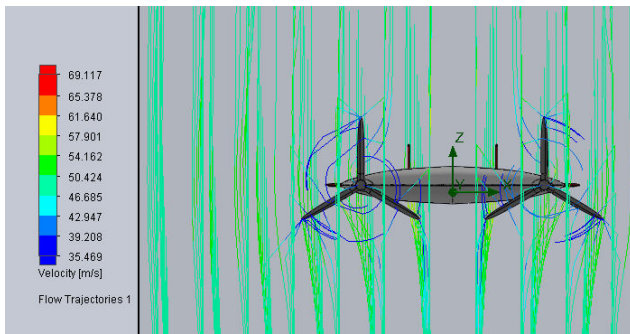


**Figure-6.** Flow trajectories for AOA=30°.

As it can be seen from figures 6 and 7, the V173 behaves extremely well also at relatively high AOA.

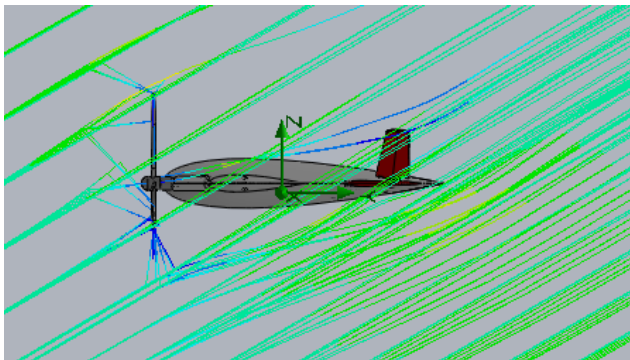


**Figure-7.** Flow trajectories for AOA=30°.

#### Influence of the propeller wake on the V173 at high AOA

At that time, the V173 appeared to be an aircraft of interest not only for its STOL capabilities but also for the characteristic of being able to reach very high AOA. From the feedback of the main pilot of the Pancake (B.T. Guyton), it appeared that the V173 could reach controlled AOA up to 45°.

In this paper it was then decided to investigate the curves of lift and resistance with and without propeller near the stall condition.

During the simulations of the V173 without propellers and no additional components improving the lift (retracted flaps) it was possible to draw  $C_L$  and  $C_D$  curves up to 50° (Figure-8)

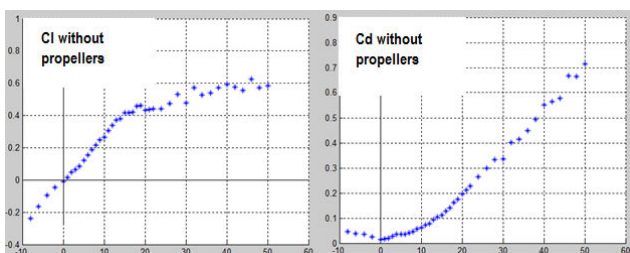


**Figure-8.**  $C_L/C_D$ -AOA without propellers.

It can be observed that for angles of attack near that stall there is a decrease of the lift with an increase of the scattering of  $C_L$  values. This behavior derives from the fact that, for AOA larger than the stall, the entire dorsal surface of the aircraft is subject to flow separation. This fact provokes a non-uniform pattern which causes a further generation of lift at the expense of the drag, which increases considerably.

This after stall behavior of the V173 without propellers is then inherently unstable with sharply varying pressure patterns and it does not allow a reliable control of the aircraft for those AOA. In fact the high turbulence on the control surfaces impair their efficiency and linearity of response.

It is then the influence of the propellers on the flow field of the plane, the reason why the pilots of Pancake could reach high AOA in flight (Figure-9).

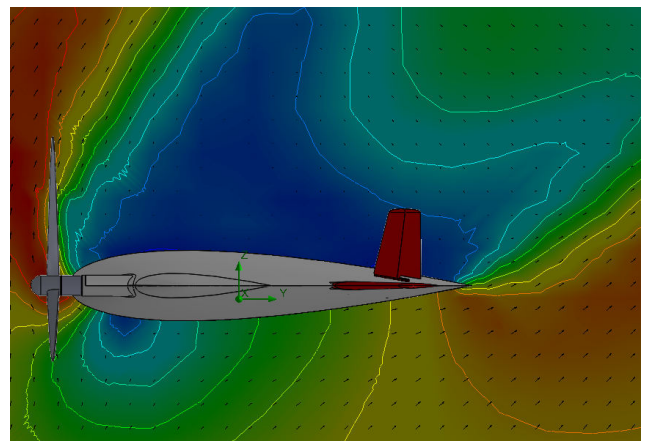


**Figure-9.** Flow separation of the powered V173 at 56°.

This condition is very well documented in Figures 10 and 11. At an AOA of 22°, the unpowered V173 is completely stalled (Figure-10) while the powered V173 displays a nearly stable normal lifting behavior without any significant flow separation (Figure-11).

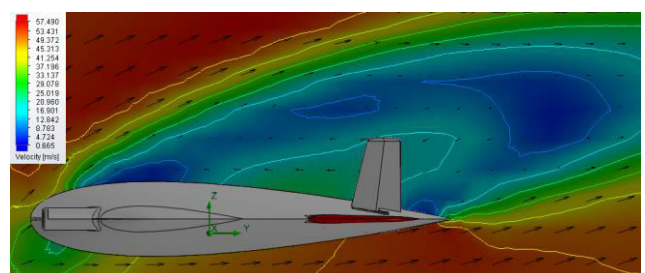


**Figure-10.** Unpowered V173 at AOA=22° with flow separation.

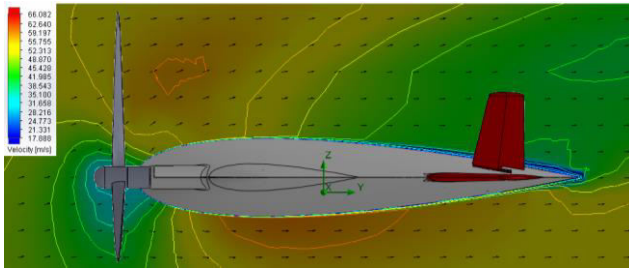


**Figure-11.** Powered V173 at AOA=22° without any flow separation.

## CONCLUSIONS

In this paper the static aerodynamic performance of an unconventional STOL aircraft like the V173 Flying Pancake was simulated. Modern CFD codes proved to be extremely effective for Lift and Drag simulation as demonstrated in previous papers.

It was also evaluated the effect of the presence in the aircraft of the two propellers of large diameter (5m) that, given the wingspan of only 7m, suggested a great influence on the performances. The propellers effect is clearly shown especially at high AOA. These results were obtained from the direct comparison of the Lift-AOA and Drag-AOA curves for the unpowered and the powered condition. The CFD results confirmed the impression of high controllability of the powered aircraft up to AOA of 50°. This behavior with the extremely smooth stall gave the impression of an aircraft impossible to stall or to spin. (L. Piancastelli et al.)

## Symbols

Symbol	Description	Unit
$\varphi_{(i,j)}$	Scalar variable linked to the tangential velocity for the cell $i,j$	-
$w_m$	Boolean weight to qualify the $m=N,E,W,S$ neighbors	-
$\varphi_m$	Scalar variable linked to the tangential velocity for neighbors of cell $i,j$	-
$h_m$	Distance between the centroids of cell $i,j$ the neighbor cell $m$	m
$p$	Exponential factor for interpolation $l=linear$	-
$\beta_m$	Weight of the neighbor cell on the cell $i,j$	-
$a_m\Phi_m$	Interpolation factors for momentum, turbulence scalar and pressure correction factors	-
$n$	Iteration number	-
$s$	Correction factor for momentum, turbulence scalar and pressure correction factors	-
$u_i$	$j$ -th component of the fluid velocity	m/s

	vector	
$\rho$	Fluid density	kg/m <sup>3</sup>
$k$	Turbulence energy	J/kg
$\epsilon$	Dissipation rate of turbulence energy	W/kg
$\mu$	Fluid viscosity	Pa s
$\tau_{i,j}$	$ij$ -th component of laminar stress tensor	Pa
$\tau_{i,j}^R$	$ij$ -th component of Reynolds stress tensor	Pa
$P_r$	Prandtl number	-
$Pr_i$	Turbulent Prandtl number	-
$C_p$	heat capacity under constant pressure	kJ/(kg K)
$T$	Temperature	K
$x_i$	$j$ -th coordinate Cartesian system	m
$n_j$	$j$ -th component of the normal to the wall in the fluid region	m
$y$	Distance from the wall along the normal to it	m
$y^+$	Dimensionless distance from the wall along the normal to it	-
$k$	Karman factor	-
$A_v$	Van drierst damping factor	-
$\delta$	Boundary layer thickness	m
$L$	Lift Force	N
$D$	Drag Force	N
$F_z$	Force along Z axis (vertical up, 3D CAD local reference system)	N
$F_z$	Force along y axis (axis of symmetry to the tail)	N
$\alpha$	AOA	degree
$\rho$	Air density	kg/m <sup>3</sup>
$S$	Wing Area	m <sup>2</sup>
$U$	TAS	m/s
$a,b,c$	Interpolating coefficient of curves	-
$V_t$	Propeller tip velocity	m/s
$n_{max}$	Max rotational speed of propeller	rpm

## REFERENCES

- [1] Gavrilouk V. N., Denisov O. P., Nakonechny V. P., Odintsov E.V., Sergienko A .A., Sobachkin A. A. 1993. Numerical Simulation of Working Processes in Rocket Engine Combustion Chamber. 44<sup>th</sup> Congress of the International Astronautical Federation, IAF-93-S.2.463, October 16-22, Graz, Austria.
- [2] Kalitzin G. and Iaccarino G. 2002. Turbulence Modeling in an Immersed-Boundary RANS-Method, Center for Turbulence Research Annual Research Briefs, Stanford University, California. pp. 415-426.



- [3] Shuvom G. 2011. Practical Flow Simulation at Highway Speeds, <http://blog.capinc.com/2011/06/practical-flow-simulation-at-highway-speeds/>.
- [4] Franke, R., 1982. Scattered data interpolation: Tests of some methods. *Math. Comput.* 38, 181-200.
- [5] Ferziger J. H. and Peric M. 2002 *Computational Methods for Fluid Dynamics*. Springer-Verlag, third-edition.
- [6] Lam C. K. G. and Bremhorst K. A. 1981. Modified Form of Model for Predicting Wall Turbulence. *ASME Journal of Fluids Engineering*. 103: 456-460.
- [7] Wilcox D. C. 1994. *Turbulence Modeling for CFD*. DCW Industries
- [8] L. Piancastelli, L. Frizziero, G. Donnici, 2014. Study and optimization of an innovative CVT concept for bikes. *Asian Research Publishing Network (ARPJ). Journal of Engineering and Applied Sciences*. ISSN 1819-6608, 9(8): 1289-1296, EBSCO Publishing, USA.
- [9] L. Piancastelli, L. Frizziero, G. Donnici, 2014. The common-rail fuel injection technique in turbocharged di-diesel-engines for aircraft applications. *Asian Research Publishing Network (ARPJ). Journal of Engineering and Applied Sciences*. ISSN 1819-6608, 9(12): 2493-2499, EBSCO Publishing, USA.
- [10] L. Piancastelli, L. Frizziero. 2015. Supercharging systems in small aircraft diesel common rail engines derived from the automotive field. *Asian Research Publishing Network (ARPJ). Journal of Engineering and Applied Sciences*. ISSN 1819-6608, 10(1): 20-26, EBSCO Publishing, USA.
- [11] L. Piancastelli, L. Frizziero. 2015. Accelerated FEM analysis for critical engine components. Published by Walailak Journal of Science and Technology The Walailak Journal of Science and Technology, Institute of Research and Development, Walailak University, ISSN: 1686-3933, Thasala, Nakhon Si Thammarat 80161. 12 (2): 151-165, Thailand.
- [12] L. Piancastelli, L. Frizziero, G. Donnici, 2015. Turbomatching of small aircraft diesel common rail engines derived from the automotive field. *Asian Research Publishing Network (ARPJ). Journal of Engineering and Applied Sciences*. ISSN 1819-6608, 10(1): 172-178, EBSCO Publishing, USA.
- [13] L. Piancastelli, L. Frizziero. 2015. Multistage turbocharging systems for high altitude flight with common rail diesel engines. *Asian Research Publishing Network (ARPJ). Journal of Engineering and Applied Sciences*. ISSN 1819-6608, 10(1): 370-375, EBSCO Publishing, USA.
- [14] L. Piancastelli, L. Frizziero. 2015. A new approach for energy recovery and turbocompounding systems for high altitude flight with common rail diesel engines. *Asian Research Publishing Network (ARPJ). Journal of Engineering and Applied Sciences*. ISSN 1819-6608, 10(2): 828-834, EBSCO Publishing, USA.
- [15] L. Piancastelli, L. Frizziero. 2015. Mapping optimization for common rail diesel conversions from the automotive to the flying applications. *Asian Research Publishing Network (ARPJ). Journal of Engineering and Applied Sciences*. ISSN 1819-6608, 10(4): 1539-1547, EBSCO Publishing, USA.
- [16] L. Piancastelli, L. Frizziero. 2015. Different approach to robust automatic control for airplanes. *Asian Research Publishing Network (ARPJ). Journal of Engineering and Applied Sciences*. ISSN 1819-6608, 10(6): 2321-2328, EBSCO Publishing, USA.
- [17] L. Piancastelli, L. Frizziero, I. Rocchi, G. Zanuccoli, N.E. Daidzic. 2013. The "C-triplex" approach to design of CFRP transport-category airplane structures. *International Journal of Heat and Technology*, ISSN 0392-8764, 31(2): 51-59.
- [18] L. Frizziero, I. Rocchi. 2013. New finite element analysis approach. Published by Pushpa Publishing House. *Far East Journal of Electronics and Communications*. ISSN: 0973-7006, 11(2): 85-100, Allahabad, India.